Precessional spin-torque dynamics in biaxial antiferromagnets

Arun Parthasarathy [*]

Department of Electrical and Computer Engineering, New York University, Brooklyn, New York 11201, USA

Egecan Cogulu [†] and Andrew D. Kent [‡]

Center for Quantum Phenomena, Department of Physics, New York University, New York, New York 10003, USA

Shaloo Rakheja [§]

Holonyak Micro and Nanotechnology Laboratory, University of Illinois at Urbana-Champaign, Urbana, Illinois 61801, USA

The Néel order of an antiferromagnet subject to a spin torque can undergo precession in a circular orbit about any chosen axis. To orient and stabilize the motion against the effects of magnetic anisotropy, the spin polarization should have components in-plane and normal to the plane of the orbit, where the latter must exceed a threshold. For biaxial antiferromagnets, the precessional motion is described by the equation for a damped-driven pendulum, which has hysteresis as a function of the spin current with a critical value where the period diverges. The fundamental frequency of the motion varies inversely with the damping and as $(x^p - 1)^{1/p}$, with the drive-to-criticality ratio x and the parameter $p > 2$. An approximate closed-form result for the threshold spin current is presented, which depends on the minimum cutoff frequency the orbit can support. Precession about the hard axis has zero cutoff frequency and the lowest threshold, while the easy axis has the highest cutoff. A device setup is proposed for electrical control and detection of the dynamics, which is promising to demonstrate a tunable terahertz nano-oscillator.

I. INTRODUCTION

In antiferromagnetic materials, injection of a spin current exerts spin torque on alternating spin moments, which can excite steady-state precession of the Néel order at terahertz frequencies [1]. The precession can reciprocally pump spins into an adjacent conductor [2], which may generate an oscillating sinusoidal [3] or spikelike [4] electric signal. These electrically induced antiferromagnetic oscillations could serve as compact narrowband terahertz sources and spike generators for applications in terahertz imaging and sensing [5] and in neuromorphic computing [6].

Given a source of spin current, how does the spin torque affect the dynamics of the Néel-order? In biaxial-anisotropy antiferromagnets, this problem has been studied for special cases where the spin current is polarized along either the easy or the hard anisotropy axis [7]. The description of the motion for a general angle of spin polarization and parametric study of the nonlinear dynamics are, however, unexplored, which we analyze in this paper in detail. This topic has implications for a tunable terahertz detector [8], which can filter frequencies higher than a certain cutoff frequency determined by the precession axis.

We study the precession of Néel order caused by spin torque about an arbitrary rotational axis. The equation of motion (Sec. II) permits steady-state solutions where the Néel order precesses in a circular orbit (Sec. III). The dynamics is analyzed separately as angular motion in the orbit which determines the frequency (Sec. III A) and perturbation from the orbital plane which determines the stability (Sec. III B). A schema for electrical control and detection of antiferromagnetic dynamics is presented in Sec. IV.

II. THEORETICAL FRAMEWORK

Antiferromagnets with a bipartite collinear ordering [9] are composed of two interpenetrating square lattices A and B with oppositely aligned moments. For such ordering, the thermodynamic state of the antiferromagnet in a mean-field approximation is represented by the unit vectors $\mathbf{m}_A$ and $\mathbf{m}_B$ for the sublattice spin moments, each of which has a magnetization M_s [10]. There are three significant contributions to the free energy density of an antiferromagnet: the exchange coupling of neighboring spins, the magnetocrystalline anisotropy, and the Zeeman interaction of magnetic moments with an external magnetic field.

Biaxial-anisotropy antiferromagnets are characterized by a direction of minimum energy which is "easy" for spins to orient along and an orthogonal direction of maximum energy which is "hard" for spins to orient along. Consider a monodomain film of thickness d_a with the easy and hard axes oriented along the unit vectors $\mathbf{u}_e$ and $\mathbf{u}_h$, respectively

[*]arun.parth@nyu.edu
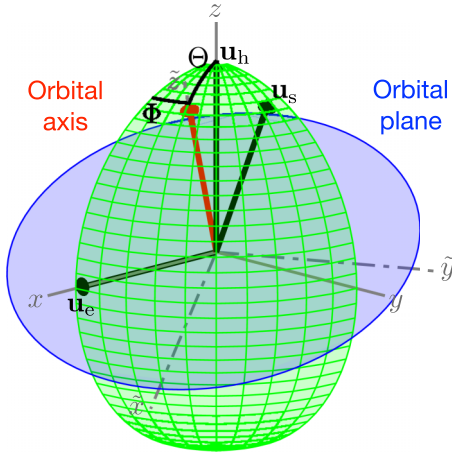[†]egecancogulu@nyu.edu
[‡]andy.kent@nyu.edu
[§]rakheja@illinois.edu

FIG. 1. Representation of magnetic-anisotropy easy axis $\mathbf{u}_e$ and hard axis $\mathbf{u}_h$, spin-polarization direction $\mathbf{u}_s$, and steady-state circular orbit of Néel order on a unit-sphere quadrant.

(Fig. 1). If the antiferromagnetic exchange coupling between the sublattice moments is much stronger than the anisotropy, the average net moment $\mathbf{m} = (\mathbf{m}_A + \mathbf{m}_B)/2$ and the Néel order $\mathbf{n} = (\mathbf{m}_A - \mathbf{m}_B)/2$ satisfy the relation $\mathbf{n}^2 = 1 - \mathbf{m}^2 \approx 1$. The total free energy density in the presence of an external magnetic field H applied along the unit vector $\mathbf{h}$ up to lowest order is [11,12]

$$\mathcal{F} = \mathcal{J}\mathbf{m}^2 + \mathcal{K}_h(\mathbf{n}\cdot\mathbf{u}_h)^2 - \mathcal{K}_e(\mathbf{n}\cdot\mathbf{u}_e)^2 - 2\mathcal{Z}\mathbf{m}\cdot\mathbf{h}, \quad (1)$$

where the exchange coupling $\mathcal{J}$, the anisotropy coefficients $\mathcal{K}_i$, and the Zeeman energy density $\mathcal{Z} = \mu_0 M_s H$ are positive numbers, and $\mathcal{J} \gg \mathcal{K}_i, \mathcal{Z}$.

In the limit of large exchange, the problem of coupled dynamics of the sublattice moments approximately reduces to motion of the Néel order on a unit-sphere phase space [13,14]. Starting from the Landau-Lifshitz-Gilbert equation augmented with the antidampinglike torque [15–17] induced by a spin current, the σ-model equation of motion for the Néel order is [12,13]

$$\mathbf{n} \times \left[\frac{M_s}{\gamma\mathcal{J}}\ddot{\mathbf{n}} + \alpha\dot{\mathbf{n}} + \frac{\gamma}{M_s}[\mathcal{K}_h(\mathbf{n}\cdot\mathbf{u}_h)\mathbf{u}_h - \mathcal{K}_e(\mathbf{n}\cdot\mathbf{u}_e)\mathbf{u}_e] \right.$$
$$\left. + \frac{\mathcal{Z}}{\mathcal{J}}[2\dot{\mathbf{n}}\times\mathbf{h} + \gamma\mu_0 H(\mathbf{n}\cdot\mathbf{h})\mathbf{h}] + \frac{\gamma J_s}{M_s d_a}(\mathbf{n}\times\mathbf{u}_s) \right] = 0, \quad (2)$$

where an overdot denotes derivative with respect to time t, $\alpha > 0$ is the Gilbert damping, γ is the absolute value of the gyromagnetic ratio, and J_s is the injected spin-current density with nonequilibrium spin polarization along the unit vector $\mathbf{u}_s$ [18]. The equation is second order, implying that the Néel order has inertia. The net moment [12]

$$\mathbf{m} = \frac{M_s}{\gamma\mathcal{J}}(\dot{\mathbf{n}}\times\mathbf{n}) + \frac{\mathcal{Z}}{\mathcal{J}}[\mathbf{h} - (\mathbf{n}\cdot\mathbf{h})\mathbf{n}] \quad (3)$$

becomes a dependent variable, allowing for the Néel order dynamics (2) to be solved independently.

Multiplying Eq. (2) by $M_s/(\gamma\mathcal{K}_e)$, when the external field is much smaller than the spin-flop field $\mathcal{Z} \ll \sqrt{\mathcal{J}\mathcal{K}_e}$ [19], the

$\mathcal{Z}$-coefficient terms need not be considered. In dimensionless form, where the time is scaled by the characteristic frequency $\tau_0 = t(\gamma\sqrt{\mathcal{J}\mathcal{K}_e}/M_s)$, the equation of motion becomes

$$\mathbf{n} \times [\mathbf{n}'' + \beta_0\mathbf{n}' + \kappa(\mathbf{n}\cdot\mathbf{u}_h)\mathbf{u}_h - (\mathbf{n}\cdot\mathbf{u}_e)\mathbf{u}_e$$
$$+ \Gamma_0(\mathbf{n}\times\mathbf{u}_s)/2] = 0, \quad (4)$$

where a prime denotes derivative with respect to τ_0, and the dimensionless parameters are defined as $\beta_0 = \alpha\sqrt{\mathcal{J}/\mathcal{K}_e}$, $\kappa = \mathcal{K}_h/\mathcal{K}_e$, and $\Gamma_0 = 2J_s/(\mathcal{K}_e d_a)$. From hereafter, $\Gamma_0\mathbf{u}_s$ is called the spin-polarization vector.

III. ANALYSIS OF SOLUTION

In the steady state, Eq. (4) can have stationary solutions $\mathbf{n}' = 0$ and time-varying solutions $\mathbf{n}' \neq 0$ depending on the parameters and the initial condition. The vector product of Eq. (4) with the angular speed $\mathbf{n} \times \mathbf{n}'$ followed by the dot product with $\mathbf{n}$ produces

$$\kappa(\mathbf{n}\cdot\mathbf{u}_h)[(\mathbf{n}\times\mathbf{n}')\cdot\mathbf{u}_h] - (\mathbf{n}\cdot\mathbf{u}_e)[(\mathbf{n}\times\mathbf{n}')\cdot\mathbf{u}_e]$$
$$+ (\mathbf{n}\times\mathbf{n}')\cdot\mathbf{n}'' + \Gamma_0(\mathbf{n}'\cdot\mathbf{u}_s)/2 = 0, \quad (5)$$

the relationship between the projection of $\mathbf{u}_e$, $\mathbf{u}_h$, and $\mathbf{u}_s$ on the orthogonal vectors $\mathbf{n}$, $\mathbf{n}'$, and $\mathbf{n}\times\mathbf{n}'$.

Among time-varying solutions, we claim that $(\mathbf{n}\times\mathbf{n}')\cdot\mathbf{n}'' = 0$ is a subset wherein the Néel order precesses in a circular orbit around the origin. Let the orbital axis make a polar angle Θ from the hard axis along z and an azimuthal angle Φ from the easy axis along x as shown in Fig. 1, with the intermediate axis along y. The orthonormal basis suitable for the orbital plane is defined as $\tilde{\mathbf{x}} = [\cos\Theta\cos\Phi, \cos\Theta\sin\Phi, -\sin\Theta]$, $\tilde{\mathbf{y}} = [-\sin\Phi, \cos\Phi, 0]$, and $\tilde{\mathbf{z}} = [\sin\Theta\cos\Phi, \sin\Theta\sin\Phi, \cos\Theta]$. If the Néel order makes an angle ϕ counterclockwise from the $\tilde{\mathbf{x}}$ axis in the orbital plane and rotates with angular speed ϕ', $\mathbf{n} = \tilde{\mathbf{x}}\cos\phi + \tilde{\mathbf{y}}\sin\phi$ and $\mathbf{n}' = \phi'(-\tilde{\mathbf{x}}\sin\phi + \tilde{\mathbf{y}}\cos\phi)$. Upon substitution into Eq. (5), the orbital axis orients along (Θ, Φ) if the components of the spin-polarization vector in the orbital plane satisfy

$$\Gamma_0(\tilde{\mathbf{x}}\cdot\mathbf{u}_s) = \sin(\Theta)\sin(2\Phi), \quad (6a)$$

$$\Gamma_0(\tilde{\mathbf{y}}\cdot\mathbf{u}_s) = (\kappa + \cos^2\Phi)\sin(2\Theta), \quad (6b)$$

and $\phi' \neq 0$. This requires the perpendicular component $\Gamma_0(\tilde{\mathbf{z}}\cdot\mathbf{u}_s)$ to overcome a certain threshold to drive the motion against damping. Determining this condition requires analyzing the angular motion and stability of the orbiting Néel order.

A. Angular motion in orbit

Equation (4) implies that tangential components of $\mathbf{n}$ inside the square bracket should vanish. Equating the component $\boldsymbol{\phi} = -\tilde{\mathbf{x}}\sin\phi + \tilde{\mathbf{y}}\cos\phi$ to zero gives the angular motion in the orbital plane:

$$2\phi'' + 2\beta_0\phi' + [\cos(2\Phi) - (\kappa + \cos^2\Phi)\sin^2\Theta]\sin(2\phi)$$
$$+ [\cos\Theta\sin(2\Phi)]\cos(2\phi) = \Gamma_0(\tilde{\mathbf{z}}\cdot\mathbf{u}_s). \quad (7)$$
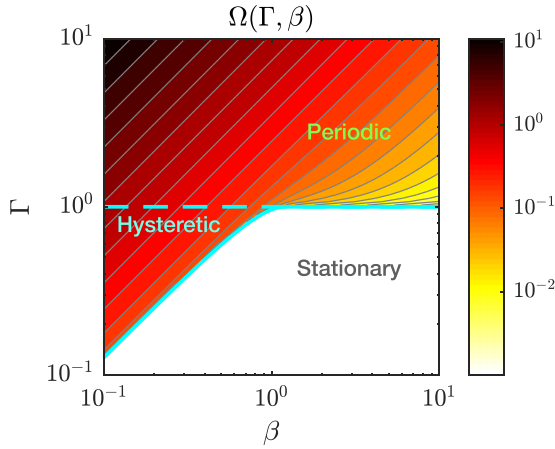
FIG. 2. Fundamental frequency Ω (16) of the damped-driven pendulum equation (9) in the parameter space of effective damping β and drive Γ represented by a contour map with values on the colorbar.

Combining the $\sin(2\phi)$ and $\cos(2\phi)$ terms together, and performing the following replacements,

$$C = \cos(2\Phi) - (\kappa + \cos^2\Phi)\sin^2\Theta, \quad D = \cos\Theta\sin(2\Phi),$$

$$g = \sqrt{C^2 + D^2}, \quad \beta = \frac{\beta_0}{\sqrt{g}}, \quad \tau = \frac{\tau_0}{\sqrt{g}}, \quad \Gamma = \frac{\Gamma_0|\tilde{\mathbf{z}}\cdot\mathbf{u}_s|}{g},$$

$$\varphi = \mathrm{sgn}(\tilde{\mathbf{z}}\cdot\mathbf{u}_s)\left[2\phi + \arctan\left(\frac{D}{C}\right)\right], \tag{8}$$

recasts the equation of motion into (derivatives denoted by prime for φ are with respect to τ)

$$\varphi'' + \beta\varphi' + \sin\varphi = \Gamma, \tag{9}$$

that of a unit-mass pendulum of unit length in effective gravity g with a viscous damping β and driven by a constant tangential force Γ [20].

The solution of the damped-driven pendulum Eq. (9) depends only on two dimensionless parameters, β and Γ. The steady-state dynamics of this nonlinear system yields either a stationary solution [$\varphi'(\tau) = 0$] or a periodic solution [$\varphi'(\tau + T) = \varphi'(\tau) \neq 0$] with a period T. Transient simulation with initial conditions $\varphi_0 = \pi$ and $\varphi_0' = 0$ over the parameter space is used to obtain the time T to complete a revolution in the steady state ($\tau > 7/\beta$). A contour plot of the fundamental frequency is shown in Fig. 2 depicting the regions of different types of solutions.

In the hysteretic region, the steady-state solution can be periodic or stationary depending on the initial conditions. For example, if the pendulum is released vertically upside down ($\varphi_0 = \pi$), then it revolves continually; but if it is released horizontally from a point where the gravity opposes the drive ($\varphi_0 = \pi/2$), then it dips and settles to equilibrium at $\sin\varphi_{\mathrm{eq}} = \Gamma$. The hysteretic region is defined as $f_h(\beta) < \Gamma(\beta) < 1$ on the domain $0 < \beta < \beta_h$, where f_h determines the homoclinic bifurcation [21]. The data are fit by a cubic polynomial,

$$f_h(\beta) = a_0\beta + \left(\frac{3 - 2a_0\beta_h}{\beta_h^2}\right)\beta^2 + \left(\frac{a_0\beta_h - 2}{\beta_h^3}\right)\beta^3, \tag{10}$$

where $a_0 = 4/\pi$ [20] and $\beta_h \approx 1.2$. The minimum threshold drive needed to sustain revolutions (solid cyan line) is

expressed as

$$\Gamma_m(\beta) = \begin{cases} f_h(\beta), & \beta < \beta_h, \\ 1, & \beta \geqslant \beta_h, \end{cases} \tag{11}$$

where $\Gamma_m = 1$ is the threshold that can initiate revolutions independent of the damping (dashed cyan line in Fig. 2).

In the overdrive limit $\Gamma \gg \Gamma_m$, the fundamental frequency is calculated by integrating Eq. (9) over a period and ignoring the role of gravity ($\sin\varphi$ term) to obtain

$$\Omega_{O\Gamma} = \frac{1}{2\pi}\frac{\Gamma}{\beta}. \tag{12}$$

This is consistent with the slope of the contour lines seen in Fig. 2 in regions far above the threshold. The time dependence of the steady-state angular speed $\omega = \varphi'$ is estimated from Eq. (9) by truncating $\sin\varphi \simeq \sin(\Gamma\tau\beta)$, multiplying by $e^{\beta\tau}$, integrating, and letting the transients decay to give

$$\omega_{O\Gamma}(\tau) \simeq \frac{\Gamma}{\beta} - \frac{\beta}{\sqrt{\beta^4 + \Gamma^2}}\sin\left(\frac{\Gamma}{\beta}\tau - \xi_{O\Gamma}\right), \tag{13}$$

where $\xi_{O\Gamma} = \arctan(\Gamma/\beta^2)$.

In the overdamped limit $\beta \gg 1$, Eq. (9) reduces to $\varphi' = (\Gamma - \sin\varphi)/\beta$, which is separable and has a closed-form integral. The periodic solution is expressed [20] as

$$\Gamma\tan\frac{\varphi_{O\beta}(\tau)}{2} = 1 + \sqrt{\Gamma^2 - 1}\tan\left(\frac{\sqrt{\Gamma^2 - 1}}{2\beta}\tau - \xi_{O\beta}\right),$$

where $\xi_{O\beta} = \arctan(1/\sqrt{\Gamma^2 - 1})$. The fundamental frequency is

$$\Omega_{O\beta} = \frac{1}{2\pi}\frac{\sqrt{\Gamma^2 - 1}}{\beta}, \tag{14}$$

and the steady-state angular speed is

$$\omega_{O\beta}(\tau) = \frac{\Gamma}{\beta} - \frac{2}{\beta}\frac{\tan(\varphi_{O\beta}/2)}{1 + \tan^2(\varphi_{O\beta}/2)}. \tag{15}$$

Superposing the overdrive limit on Eq. (15) results in convergence of solutions with Eq. (13).

For moderate drive $\Gamma \gtrsim \Gamma_m$ and damping $\beta \lesssim 1$, it is not possible to derive analytic solutions [20,22]. However, the fundamental frequency closely follows the law

$$\Omega(\Gamma, \beta) = \frac{1}{2\pi}\frac{\left[\Gamma^p - \Gamma_m^p\right]^{1/p}}{\beta}\begin{cases} \Gamma_m = \Gamma_m(\beta), \\ p = p(\beta), \end{cases} \tag{16}$$

conceived by generalizing the overdamped result (14). The functional relationship $p(\beta)$ and the accuracy of the model are depicted in Fig. 3. The inverse dependence of p on β implies that a weakly damped system $\beta \ll 1$ is much easier to oscillate than a strongly damped $\beta \gg 1$ for a fixed drive-to-threshold ratio. Superposing the overdrive limit results in convergence with Eq. (12).

To compare periodic solutions across the parameter space, the first-order term $\epsilon_{O\Gamma} = (\Gamma_m/\Gamma)^p/p$ in the expansion of $2\pi\beta\Omega/\Gamma$ (16) is used to measure nearness to overdrive; the relative increment $\epsilon_{th} = (\Gamma - \Gamma_m)/\Gamma_m$ is used to measure nearness to threshold. The wave forms of the angular speed for limiting cases of damping and drive are juxtaposed in Fig. 4. The closed-form solutions agree with the numerical
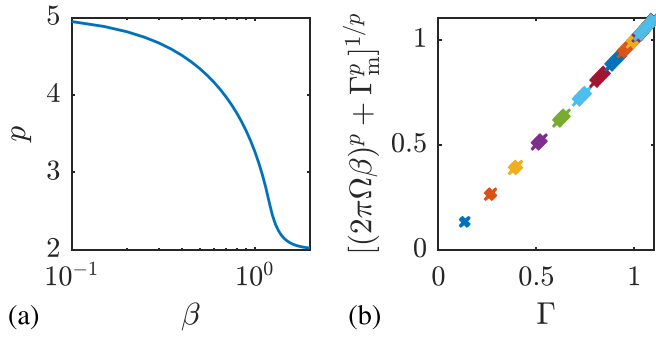
FIG. 3. Plot of Eq. (16). (a) The parameter p increases from 2 for $\beta \lesssim 1$. (b) The data for Ω evaluated with the vertical-axis function fit accurately with Γ, where adjoining markers of the same color have a unique β (decreasing diagonally up).

ones, except when the drive is near the minimum threshold and the damping is weak. The oscillations in angular speed are coherent in the overdrive limit and Dirac comb like in the overdamped limit for near-threshold drive.

B. Stability of orbit

Orbits that are elevated from the plane perpendicular to the hard axis may become stable only above a critical angular speed [23]. To study stability, the Néel order is perturbed from the orbital plane by a small angle $\delta\theta$ or $\mathbf{n} = \tilde{\mathbf{x}} \cos\phi + \tilde{\mathbf{y}} \sin\phi + \tilde{\mathbf{z}}\delta\theta$. Equating the component $\boldsymbol{\theta} = (\tilde{\mathbf{x}} \cos\phi + \tilde{\mathbf{y}} \sin\phi)\delta\theta - \tilde{\mathbf{z}}$ inside the square bracket of Eq. (4) to zero, using the relation of Eq. (6), and retaining only linear terms in $\delta\theta$ give the equation of a damped harmonic oscillator
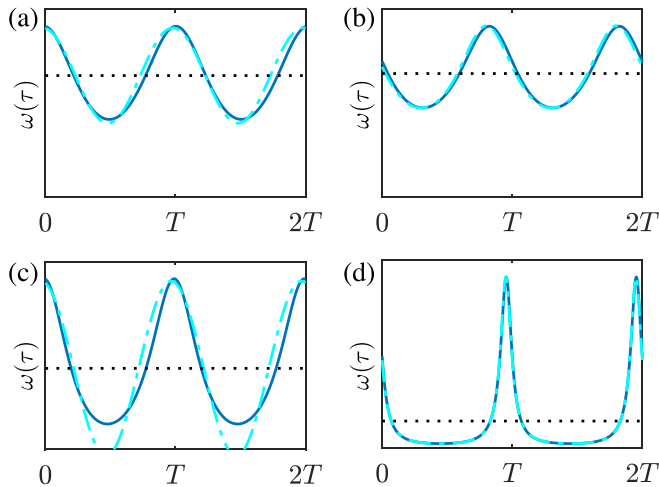

FIG. 4. Wave forms of the steady-state angular speed $\omega(\tau)$ of the damped-driven pendulum revolving with time period T for (a) overdrive $\epsilon_{\text{OF}} = 0.05$ and small damping $\beta = 0.2$, (b) overdrive $\epsilon_{\text{OF}} = 0.05$ and large damping $\beta = 5$, (c) near-threshold drive $\epsilon_{\text{th}} = 0.05$ and small damping $\beta = 0.2$, and (d) near-threshold drive $\epsilon_{\text{th}} = 0.05$ and large damping $\beta = 5$. The dark-color plot is the exact numerical solution and the light-color plot is the approximate closed-form solution. Dotted horizontal line denotes the average value equal to $2\pi\Omega$ (16). At time $\tau = 0$, the pendulum is at the lowest point, $\varphi = 0$.

$\delta\theta'' + \beta_0\delta\theta' + K\delta\theta = 0$, where the spring constant

$$K = \kappa(\cos^2\Theta - \sin^2\Theta\cos^2\phi) - \sin^2\Theta\cos^2\Phi$$
$$+ (\cos\Theta\cos\Phi\cos\phi - \sin\Phi\sin\phi)^2 + \phi'^2. \quad (17)$$

To understand how K depends on orbital parameters (8), expression (17) is expanded and compactly rewritten as

$$K = \kappa - 1 - 3\mathcal{E} + \frac{g}{2}\left(\cos\varphi + \frac{\varphi'^2}{2}\right), \quad (18)$$

where the angle-averaged energy of the orbit

$$\mathcal{E} = \langle \kappa(\mathbf{n} \cdot \mathbf{u}_{\text{h}})^2 - (\mathbf{n} \cdot \mathbf{u}_{\text{e}})^2 \rangle$$
$$= \tfrac{1}{2}[(\kappa + \cos^2\Phi)\sin^2\Theta - 1]. \quad (19)$$

If K is positive throughout the angular motion, the Néel order will be restored to the orbital plane. The precise condition for stability for a general β requires numerically evaluating the steady-state value of $(\cos\varphi + \varphi'^2/2)$ in the parameter space of β and Γ (similar to how fundamental frequency was obtained in Sec. III A) and checking if $\min_\varphi K > 0$. But, an approximate closed-form result is obtained by treating φ' as a constant average value $2\pi\Omega$ (16), which is accurate in the overdrive limit. Then, the stability condition is $\min_\varphi K = g\pi^2\Omega^2 - (g/2 + 3\mathcal{E} + 1 - \kappa) > 0$, which gives the minimum angular frequency

$$\omega_0 = \text{Re}(\sqrt{g/2 + 3\mathcal{E} + 1 - \kappa}), \quad (20)$$

which is positive for orientations satisfying $g/2 + 3\mathcal{E} + 1 - \kappa > 0$ (Fig. 5). The stability threshold for perpendicular projection of the spin-polarization vector is

$$(\Gamma_0|\tilde{\mathbf{z}} \cdot \mathbf{u}_{\text{s}}|)_{\text{th}} = [(2\beta_0\omega_0)^p + \{g\Gamma_{\text{m}}(\beta_0/\sqrt{g})\}^p]^{1/p}, \quad (21)$$

where $p = p(\beta_0/\sqrt{g})$ [Fig. 3(a)].

In essence, to orient and stabilize the orbital motion about an axis (Θ, Φ) requires the spin-polarization vector

$$\Gamma_0\mathbf{u}_{\text{s}} = \sin(\Theta)\sin(2\Phi)\tilde{\mathbf{x}} + (\kappa + \cos^2\Phi)\sin(2\Theta)\tilde{\mathbf{y}}$$
$$+ \Gamma_0(\tilde{\mathbf{z}} \cdot \mathbf{u}_{\text{s}})\tilde{\mathbf{z}}, \quad (22)$$

where Γ_0 should exceed the threshold

$$\Gamma_{0,\text{th}} = \big[\sin^2(\Theta)\sin^2(2\Phi) + (\kappa + \cos^2\Phi)^2\sin^2(2\Theta)$$
$$+ (\Gamma_0|\tilde{\mathbf{z}} \cdot \mathbf{u}_{\text{s}}|)_{\text{th}}^2\big]^{1/2}. \quad (23)$$

The spin-polarization direction does not coincide with the orbital axis, except for directions along the anisotropy axes for which $\Gamma_{0,\text{th}} = (\Gamma_0|\tilde{\mathbf{z}} \cdot \mathbf{u}_{\text{s}}|)_{\text{th}}$. The orbital parameters to orient along the anisotropy axes are as follows: the hard axis has $(\Theta, \Phi) = (0, \Phi)$, $g = 1$, and $\omega_0 = 0$; the intermediate axis has $(\Theta, \Phi) = (\pi/2, \pi/2)$, $g = \kappa + 1$, and $\omega_0 = \sqrt{\kappa}$; and the easy axis has $(\Theta, \Phi) = (\pi/2, 0)$, $g = \kappa$, and $\omega_0 = \sqrt{\kappa + 1}$. The hard axis supports an orbit with the lowest threshold and minimum angular frequency, while the easy axis has the highest cutoff. The axis along $(\Theta, \Phi) = [\arctan(1/\sqrt{\kappa}), 0]$ has $g = 0$, meaning no oscillations in angular speed. For small damping, the range of threshold varies from $4\beta_0/\pi$ to $\kappa + 1$ (Fig. 5).

Below the threshold spin current, for moderate values of damping, the Néel-order motion can become chaotic (aperiodic long-term behavior) for a small window of current,
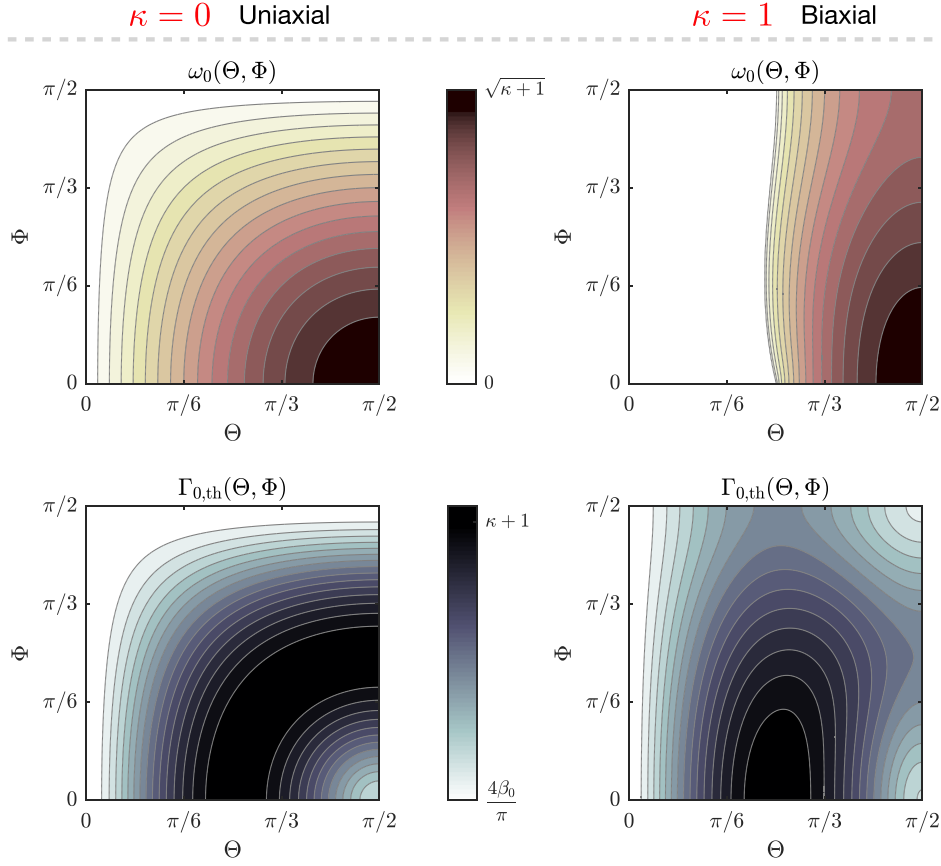
FIG. 5. The minimum angular frequency ω_0 (top panels) and the threshold spin current $\Gamma_{0,\text{th}}$ (bottom panels) which can orient and stabilize the orbital motion of the Néel order about an axis (Θ, Φ) when damping is small $\beta_0 = 0.2$ for uniaxial (left panels) and biaxial (right panels) anisotropy, represented by contour maps with the range of values on the colorbar (middle). The minimum frequency ω_0 increases with deviation from the hard axis $(\Theta, \Phi) = (0, \Phi)$ and peaks along the easy axis $(\Theta, \Phi) = (\pi/2, 0)$. The threshold is lowest for motion about the hard axis and peaks for an intermediate orientation in-between hard and easy axes.

before settling down to equilibrium, which will be the subject of future research.

Thus, the choice of the orbital axis and the parameters of damping and anisotropy determine the threshold current, cutoff frequency, and wave form of the angular speed of the Néel order. These mathematical results may be translated into electrically measurable input and output signals via the device setup presented in the next section.

IV. ELECTRICAL CONTROL AND DETECTION

Electrical means of controlling the spin current injected into the antiferromagnet and detecting the resulting oscillations in a thin-film system are fundamental to spintronic devices and applications in technology. In this regard, the setup should be all electric with a controllable spin-polarization direction.

Pure spin current through an insulating antiferromagnetic layer can be generated from electric current flowing in an overlaid lateral spin valve or spin Hall structure. In the lateral spin valve structure shown in Fig. 6(a), electric current across the ferromagnetic reference layers injects spin accumulation in the normal metal and spin current in the antiferromagnet, polarized parallel to the reference-layer magnetization

[24], which can be oriented along the desired direction by a magnetic field. In the spin Hall structure shown in Fig. 6(b), the electric current in the heavy metal with strong spin-orbit coupling produces a perpendicular spin current polarized transverse to the electric current in the film plane [16]. The spin Hall effect can be efficient in converting electric current to spin, but the spin polarization is constrained within the plane. However, a spin-source material with reduced crystalline symmetry [25] or the planar Hall effect in a ferromagnet lifts this restriction [26], which allows for a controllable spin-polarization direction.

For the choice of spin polarization along the hard axis of the antiferromagnetic layer, the viable geometries are the in-plane-anisotropy antiferromagnet with the lateral spin valve structure made of a perpendicular reference-layer magnetization and the perpendicular-anisotropy antiferromagnet with the spin Hall structure in which the in-plane electric current is transverse to the in-plane hard axis. For both the geometries, the input is a constant-current source, the back diffusion ("backflow") of injected spins [27] is considered small, and the output is detected under open-circuit conditions.

To excite and control Néel-order precession, the spin current must exert adequate antidampinglike torque. The threshold spin-current density that initiates precession is
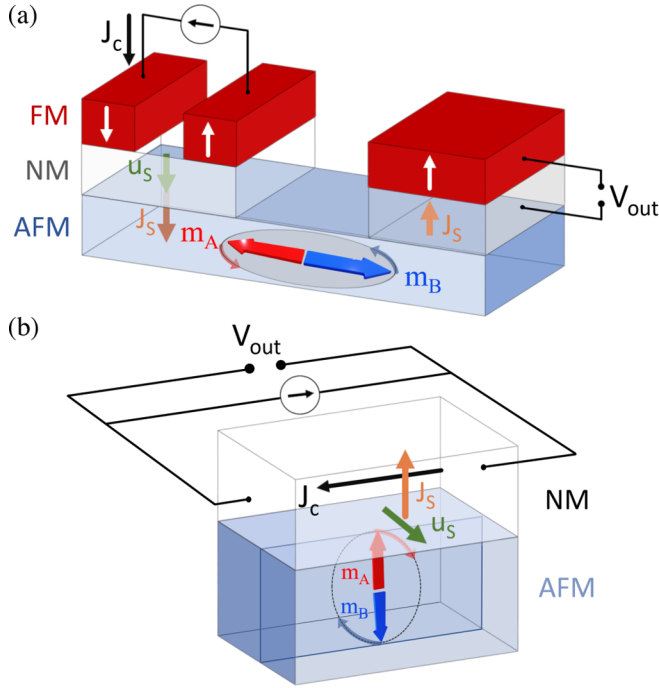
FIG. 6. Device setup for electrical control and detection of terahertz oscillations in thin-film antiferromagnetic insulators. (a) In-plane spin valve geometry: Lateral spin valve structure made of a perpendicular reference-layer magnetization on top of an in-plane-anisotropy antiferromagnet. (b) Perpendicular spin Hall geometry: Spin Hall structure with in-plane electric current transverse to the in-plane hard axis on top of a perpendicular-anisotropy antiferromagnet. Input electric current J_c is converted into a pure spin current J_s polarized u_s along the hard-anisotropy axis to cause precession of the sublattice moments m_A and m_B, which pumps spin current back to generate an oscillating voltage signal at the output V_{out}. FM, ferromagnet; NM, normal metal; AFM, antiferromagnet.

obtained from the condition $\Gamma_{th} = 1$ (11) as $J_{s,th} = \mathcal{K}_e d_a / 2$. The corresponding electric-current density depends on the specific geometry. For the in-plane spin valve geometry, assuming low spin-memory loss in the normal metal, the conversion from electric current to spin is determined by the conductance of majority- and minority-spin electrons g_M and g_m, respectively, and the spin-mixing conductance at the interface of normal metal and antiferromagnet g_r. The threshold electric-current density is [28]

$$J_{c,th}^{ip\text{-}valv} = \frac{2e}{\hbar} \frac{(g_r + g_M + g_m)(g_M + g_m)}{g_r(g_M - g_m)} J_{s,th}. \quad (24)$$

For the perpendicular spin Hall geometry, the conversion from electric current to spin is determined by the spin Hall angle Θ_s, the layer thickness d_n, the spin diffusion length λ, the conductivity σ of the heavy metal, and the spin-mixing conductance at the interface of the heavy metal and the antiferromagnet g_r. The threshold electric-current density is [29]

$$J_{c,th}^{pe\text{-}Hall} = \frac{e}{\hbar} \frac{\sigma}{\lambda g_r} \frac{\coth(d_n/2\lambda)}{\Theta_s} J_{s,th}. \quad (25)$$

If the effective damping $\beta \ll 1$, the minimum current for sustaining precession is about $1/\beta$ times lower, as seen from

TABLE I. Properties of bulk NiO and Cr_2O_3 at 300 K.

Parameter	NiO	Ref.	Cr_2O_3	Ref.
$\mathcal{J}$ (J/m^3)	3.4×10^8	[3,32]	9.5×10^7	[33,34]
$\mathcal{K}_e$ (J/m^3)	2.2×10^4	[3,32]	3.2×10^3	[33,34]
$\mathcal{K}_h$ (J/m^3)	5.5×10^5	[3,32]	≈ 0	[33,34]
M_s (A/m)	3.5×10^5	[3,35]	1.9×10^5	[33,34]
α_0	6×10^{-4}	[3,35]	2×10^{-4}	[33,36]

Fig. 2 and Eq. (11). Lowering the current drive after initiation mitigates excessive Joule heating in the metal and allows for tunability of oscillation to subterahertz frequencies detectable by microelectronic circuits.

The precessing Néel order can reciprocally pump time-varying spin current $\propto \mathbf{n} \times \mathbf{n}'$ back into the adjacent metal and experience a dampinglike backaction [30]. This virtually enhances the Gilbert damping expressed as $\alpha = \alpha_0 + \alpha_s$, where α_0 is the intrinsic damping constant and the enhancement [29]

$$\alpha_s = \frac{\hbar^2 \gamma g_r}{2e^2 M_s d_a}. \quad (26)$$

The pumped spin current is converted into voltage under open-circuit conditions via spin filtering for the in-plane spin valve geometry and via the inverse spin Hall effect for the perpendicular spin Hall geometry. The voltage signal generated at the output of each geometry is [28,31]

$$V_{out}^{ip\text{-}valv}(t) = \frac{\hbar \gamma \sqrt{\mathcal{J}\mathcal{K}_e}}{2eM_s} \frac{g_r(g_M - g_m)\omega(t)}{(g_r + g_M + g_m)(g_M + g_m)}, \quad (27)$$

$$V_{out}^{pe\text{-}Hall}(t) = \frac{\hbar \gamma \sqrt{\mathcal{J}\mathcal{K}_e}}{2eM_s} \frac{\lambda g_r}{\sigma} \Theta_s \tanh\left(\frac{d_n}{2\lambda}\right)\omega(t), \quad (28)$$

where ω is the dimensionless angular frequency (Sec. III A).

Bipartite collinear antiferromagnets such as NiO and Cr_2O_3 are insulators, whose bulk magnetic properties are well studied (Table I). For thin films, density functional theory predicts that NiO(001) on $SrTiO_3$ substrate has an in-plane anisotropy [38], and experiments have shown that Cr_2O_3(0001) on Al_2O_3 substrate has a perpendicular anisotropy [39], but measurement of magnetic anisotropy of antiferromagnetic films is less explored [40]. The magnetic anisotropy of thin films and multilayers can significantly differ from bulk magnetic materials due to epitaxial strain from substrate and reduced local symmetry of surface atoms [41]. The magnetic anisotropy energy is augmented by magnetostrictive and surface anisotropies which can elicit an in-plane or a perpendicular spin orientation independent of the specific growth direction of the film [42]. Nonetheless, we consider the bulk properties to estimate specifications for the proposed setup.

For characteristic values of geometry parameters (Table II), the threshold current density $J_{c,th}^{ip\text{-}valv} \approx 2 \times 10^7$ A/cm^2 and $J_{c,th}^{pe\text{-}Hall} \approx 10^8$ A/cm^2; the effective damping $\beta^{ip\text{-}valv} = 0.18$ and $\beta^{pe\text{-}Hall} = 0.24$; the frequency scale is 1.4 THz for NiO and 0.5 THz for Cr_2O_3; and the amplitude of alternating output signal $v_{out}^{ip\text{-}valv} = 70$ μV and $v_{out}^{pe\text{-}Hall} = 0.4$ μV at the threshold current [43]. The specifications are promising

TABLE II. Characteristics of device geometry.

Parameter	Layer info	Ref.
$g_M = 10^{10}$ (S/m^2)	NM/FM	[28]
$g_m = 10^9$ (S/m^2)	NM/FM	[28]
$g_r = 10^{14}$ (S/m^2)	NM/AFM	[37]
$d_a = 5$ nm	AFM	[3]
$\sigma = 10^6$ (S/m)	NM (Pt)	[3]
$d_n = 20$ nm	NM (Pt)	[3]
$\lambda = 7$ nm	NM (Pt)	[3]
$\Theta_s = 0.1$	NM (Pt)	[3]

for practical demonstration of a terahertz signal emitter at nanoscale lengths.

Additionally, the setup can detect terahertz radiation by phase locking if the antiferromagnet's crystal symmetry allows for staggered-field Néel spin-orbit torque, which includes materials such as CuMnAs and Mn$_2$Au [8]. By changing the spin-polarization angle and the threshold spin-current density from $2J_{s,th}/d_a \propto \alpha \sqrt{\mathcal{J}\mathcal{K}_e}$ to $\mathcal{K}_e + \mathcal{K}_h$ (22), and hence the precession axis, the minimum angular frequency ω_0 can be tuned from zero to $\sqrt{\kappa + 1}$. This method proportionally shifts the center of the phase-locking interval. Frequencies below ω_0 are cut off and this system acts as a high-pass filter operating in the terahertz range. For this scheme to work, one faces the practical challenge of how to generate adequate spin current. Reducing the magnetic anisotropy of the antiferromagnet by strain engineering [44], or enhancing the spin current by replacing the heavy metal with a topological insulator [45], or a combination of both might be helpful.

V. CONCLUSION

We studied the equation of motion of the Néel order of an antiferromagnet under the action of spin torque for steady-state solution, which involves precession in a circular orbit about an axis oriented along a general direction. The required components of the spin-polarization vector in the orbital plane are explicit functions of the axis orientation. We analyzed the dynamics by bisecting it into angular motion in the orbit and perturbation from the orbital plane.

The angular motion reduces to an equation of a damped-driven pendulum described by two parameters which represent the effective damping and drive. The parameter space is explored to identify regions of periodicity, hysteresis, and infinite-period bifurcation. Solutions for oscillations in angular velocity are derived when the damping and drive are separately large and a function for the fundamental frequency is found. The oscillations are sinusoidal for large drive and spikelike for large damping near threshold.

The perturbing elevation from the orbital plane reduces to an equation of a damped harmonic oscillator with an effective spring constant. The stability condition introduces a minimum cutoff frequency for orbits, which is used to calculate the threshold spin current. Orbital axes which deviate sufficiently from the hard axis have nonzero cutoff frequency, increasing monotonically with the highest value for the easy-axis direction. The threshold is lowest along the hard axis, which varies nonmonotonically with the angle from the hard axis for small damping.

Finally, we proposed device setups for electrical control and detection of terahertz oscillations in thin-film antiferromagnets and show how to practically achieve arbitrary precessional axis orientations.

[1] E. Gomonay and V. Loktev, Spintronics of antiferromagnetic systems, J. Low Temp. Phys. **40**, 17 (2014).

[2] P. Vaidya, S. A. Morley, J. van Tol, Y. Liu, R. Cheng, A. Brataas, D. Lederman, and E. Del Barco, Subterahertz spin pumping from an insulating antiferromagnet, Science **368**, 160 (2020).

[3] R. Khymyn, I. Lisenkov, V. Tiberkevich, B. A. Ivanov, and A. Slavin, Antiferromagnetic THz-frequency Josephson-like oscillator driven by spin current, Sci. Rep. **7**, 43705 (2017).

[4] R. Khymyn, I. Lisenkov, J. Voorheis, O. Sulymenko, O. Prokopenko, V. Tiberkevich, J. Akerman, and A. Slavin, Ultrafast artificial neuron: Generation of picosecond-duration spikes in a current-driven antiferromagnetic auto-oscillator, Sci. Rep. **8**, 15727 (2018).

[5] D. M. Mittleman, Perspective: Terahertz science and technology, J. Appl. Phys. **122**, 230901 (2017).

[6] J. Torrejon, M. Riou, F. A. Araujo, S. Tsunegi, G. Khalsa, D. Querlioz, P. Bortolotti, V. Cros, K. Yakushiji, A. Fukushima

et al., Neuromorphic computing with nanoscale spintronic oscillators, Nature (London) **547**, 428 (2017).

[7] The algebraic expression for the threshold drive is known in the limit of small [3] and large [4] damping. An expression for the time dependence of the angular speed was found for large drive and small damping [3]. The influence of dissipative spin-orbit torque [46] was studied for the case of easy-plane anisotropy.

[8] O. Gomonay, T. Jungwirth, and J. Sinova, Narrow-band tunable terahertz detector in antiferromagnets via staggered-field and antidamping torques, Phys. Rev. B **98**, 104430 (2018).

[9] T. Dombre and N. Read, Nonlinear σ models for triangular quantum antiferromagnets, Phys. Rev. B **39**, 6797 (1989).

[10] C. Kittel, Introduction to Solid State Physics (Wiley, New York, 2004).

[11] A. Qaiumzadeh, H. Skarsvåg, C. Holmqvist, and A. Brataas, Spin Superfluidity in Biaxial Antiferromagnetic Insulators, Phys. Rev. Lett. **118**, 137201 (2017).

[12] A. Parthasarathy and S. Rakheja, Phenomenological description of the dynamics of bipartite antiferromagnets in the limit of strong exchange, arXiv:1904.03529.

[13] A. Kosevich, B. Ivanov, and A. Kovalev, Magnetic solitons, Phys. Rep. **194**, 117 (1990).

[14] H. V. Gomonay and V. M. Loktev, Spin transfer and current-induced switching in antiferromagnets, Phys. Rev. B **81**, 144427 (2010).

[15] J. Slonczewski, Current-driven excitation of magnetic multilayers, J. Magn. Magn. Mater. **159**, L1 (1996).

[16] J. Sinova, S. O. Valenzuela, J. Wunderlich, C. H. Back, and T. Jungwirth, Spin Hall effects, Rev. Mod. Phys. **87**, 1213 (2015).

[17] T. Jungwirth, X. Marti, P. Wadley, and J. Wunderlich, Antiferromagnetic spintronics, Nat. Nanotechnol. **11**, 231 (2016).

[18] $J_s > 0$ in the sense of electrons with spin-polarization direction $\mathbf{u}_s$ (or $-\mathbf{u}_s$) injecting into (or ejecting from) the magnetic material.

[19] The spin-flop field is around ~ 10 T for antiferromagnetic insulators such as NiO [47], Cr_2O_3 [48], and MnF_2 [49].

[20] P. Coullet, J. M. Gilli, M. Monticelli, and N. Vandenberghe, A damped pendulum forced with a constant torque, Am. J. Phys. **73**, 1122 (2005).

[21] S. H. Strogatz, *Nonlinear Dynamics and Chaos* (CRC, Boca Raton, FL, 2018).

[22] M. Gitterman, *The Noisy Pendulum* (World Scientific, Singapore, 2008).

[23] Similar to the Round Up amusement ride which has to spin fast enough when the circular horizontal platform rises so that the centrifugal force is able to push riders against the wall and prevent them from falling.

[24] F. J. Jedema, A. Filip, and B. Van Wees, Electrical spin injection and accumulation at room temperature in an all-metal mesoscopic spin valve, Nature (London) **410**, 345 (2001).

[25] D. MacNeill, G. Stiehl, M. Guimaraes, R. Buhrman, J. Park, and D. Ralph, Control of spin–orbit torques through crystal symmetry in WTe_2/ferromagnet bilayers, Nat. Phys. **13**, 300 (2017).

[26] C. Safranski, J. Z. Sun, J.-W. Xu, and A. D. Kent, Planar Hall Driven Torque in a Ferromagnet/Nonmagnet/Ferromagnet System, Phys. Rev. Lett. **124**, 197204 (2020).

[27] H. J. Jiao and G. E. W. Bauer, Spin Backflow and ac Voltage Generation by Spin Pumping and the Inverse Spin Hall Effect, Phys. Rev. Lett. **110**, 217602 (2013).

[28] H. Skarsvåg, C. Holmqvist, and A. Brataas, Spin Superfluidity and Long-Range Transport in Thin-Film Ferromagnets, Phys. Rev. Lett. **115**, 237201 (2015).

[29] R. Cheng, J.-G. Zhu, and D. Xiao, Dynamic Feedback in Ferromagnet–Spin Hall Metal Heterostructures, Phys. Rev. Lett. **117**, 097202 (2016).

[30] R. Cheng, J. Xiao, Q. Niu, and A. Brataas, Spin Pumping and Spin-Transfer Torques in Antiferromagnets, Phys. Rev. Lett. **113**, 057601 (2014).

[31] R. Cheng, D. Xiao, and A. Brataas, Terahertz Antiferromagnetic Spin Hall Nano-Oscillator, Phys. Rev. Lett. **116**, 207603 (2016).

[32] A. Sievers III and M. Tinkham, Far infrared antiferromagnetic resonance in MnO and NiO, Phys. Rev. **129**, 1566 (1963).

[33] A. Parthasarathy and S. Rakheja, Dynamics of Magnetoelectric Reversal of an Antiferromagnetic Domain, Phys. Rev. Appl. **11**, 034051 (2019).

[34] S. Foner, High-field antiferromagnetic resonance in Cr_2O_3, Phys. Rev. **130**, 183 (1963).

[35] M. T. Hutchings and E. Samuelsen, Measurement of spin-wave dispersion in NiO by inelastic neutron scattering and its relation to magnetic properties, Phys. Rev. B **6**, 3447 (1972).

[36] E. Samuelsen, M. Hutchings, and G. Shirane, Inelastic neutron scattering investigation of spin waves and magnetic interactions in Cr_2O_3, Physica **48**, 13 (1970).

[37] L. Baldrati, A. Ross, T. Niizeki, C. Schneider, R. Ramos, J. Cramer, O. Gomonay, M. Filianina, T. Savchenko, D. Heinze *et al.*, Full angular dependence of the spin Hall and ordinary magnetoresistance in epitaxial antiferromagnetic NiO(001)/Pt thin films, Phys. Rev. B **98**, 024422 (2018).

[38] X. Z. Chen, R. Zarzuela, J. Zhang, C. Song, X. F. Zhou, G. Y. Shi, F. Li, H. A. Zhou, W. J. Jiang, F. Pan, and Y. Tserkovnyak, Antidamping-Torque-Induced Switching in Biaxial Antiferromagnetic Insulators, Phys. Rev. Lett. **120**, 207204 (2018).

[39] N. Wu, X. He, A. L. Wysocki, U. Lanke, T. Komesu, K. D. Belashchenko, C. Binek, and P. A. Dowben, Imaging and Control of Surface Magnetization Domains in a Magnetoelectric Antiferromagnet, Phys. Rev. Lett. **106**, 087202 (2011).

[40] T. Jungwirth, J. Sinova, A. Manchon, X. Marti, J. Wunderlich, and C. Felser, The multiple directions of antiferromagnetic spintronics, Nat. Phys. **14**, 200 (2018).

[41] D. Sander, The magnetic anisotropy and spin reorientation of nanostructures and nanoscale films, J. Phys. Condens. Matter **16**, R603 (2004).

[42] K. Krishnan, *Fundamentals and Applications of Magnetic Materials* (Oxford University, Oxford, 2016).

[43] The AC signal is obtained by calculating the coefficient of the sinusoidal term in Eq. (13).

[44] Z. Liu, Z. Feng, H. Yan, X. Wang, X. Zhou, P. Qin, H. Guo, R. Yu, and C. Jiang, Antiferromagnetic piezospintronics, Adv. Electron. Mater. **5**, 1900176 (2019).

[45] S. M. Farzaneh and S. Rakheja, Intrinsic spin Hall effect in topological insulators: A first-principles study, Phys. Rev. Materials **4**, 114202 (2020).

[46] R. E. Troncoso, K. Rode, P. Stamenov, J. M. D. Coey, and A. Brataas, Antiferromagnetic single-layer spin-orbit torque oscillators, Phys. Rev. B **99**, 054433 (2019).

[47] H. Wiegelmann, A. Jansen, P. Wyder, J.-P. Rivera, and H. Schmid, Magnetoelectric effect of Cr_2O_3 in strong static magnetic fields, Ferroelectrics **162**, 141 (1994).

[48] F. L. A. Machado, P. R. T. Ribeiro, J. Holanda, R. L. Rodríguez-Suárez, A. Azevedo, and S. M. Rezende, Spin-flop transition in the easy-plane antiferromagnet nickel oxide, Phys. Rev. B **95**, 104418 (2017).

[49] I. Jacobs, Spin-flopping in MnF_2 by high magnetic fields, J. Appl. Phys. **32**, S61 (1961).